Composites: Part A 167 (2023) 107421

Contents lists available at ScienceDirect

Composites Part A

journal homepage: www.elsevier.com/locate/compositesa

Modeling of yarn interactions for non-axisymmetric biaxial overbraiding simulations

A.N. Vu *, W.J.B. Grouve, R. Akkerman *

Chair of Production Technology, Department of Mechanics of Solids, Surfaces and Systems, University of Twente, P.O. Box 217, NL-7500 AE Enschede, The Netherlands

ARTICLE INFO

Keywords:
E. Braiding
C. Process modeling
A. Preform
E. Automation

ABSTRACT

Overbraiding is an efficient manufacturing process for complex composite preforms. Process simulations to predict the braid angle and coverage are useful when designing braid reinforced products. It is known that neglecting yarn interaction in such simulations leads to an incorrect prediction of the braiding angle and cover factor of the braid. This study reports a new yarn interaction model to simulate the biaxial overbraiding process for non-axisymmetric and complex preforms. An Eulerian on Lagrangian approach is used, allowing the stick and slip process to be resolved at each point of contact. A fast frontal approach is implemented to account for the multiple interlaced points. Validations for different biaxial cases are presented, obtaining good agreement with previous experiments. Numerical tests show that the braid angle and the convergence zone length are significantly affected by the coefficient of friction until reaching the steady state where the braid angle is unchanged with time.

1. Introduction

Overbraiding is a textile manufacturing technology that can be used to manufacture hollow preforms for composite applications [1–3]. The process offers a high fiber deposition rate and can be automated to a large extent [4]. The highly interlaced structure of the braid allows coverage of complex mandrel shapes, with for example non-circular cross-sections and sharp curvatures [5]. In addition, the braid structure also minimizes crack growth and improves delamination resistance, making them good impact strength components [6]. Because of its advantages, the braiding process is utilized in various industrial applications, including aerospace and automotive [7]. Overbraiding is typically part of a composite production process that includes resin transfer molding in which the preform is usually impregnated and cured with a thermoset resin [8]. The impregnation process is strongly affected by the preform, particularly the local fiber content, the thickness distribution, as well as the fiber orientation.

1.1. Process definition

The overbraiding process is schematically illustrated in Fig. 1(top). Typically, a traverse moves the mandrel through the spool circle and the guide ring with an axial take-up velocity v, whilst the other components are fixed. The traverse may have additional degrees of freedom to allow for a curved centerline or other more complex geometric features. The warp and weft spools, referred to as bias yarn groups, move around the spool circle on carriers. The warp spools move clockwise, while weft spools move counter-clockwise. Both groups have the same average angular velocity ω around the process axis. The spool carriers are passed between the slots of horn gears and follow a serpentine path as shown in Fig. 1(bottom). The spool path determines the interlace structure or the braid pattern of the preform. The most common braid patterns used in biaxial overbraiding are 1/1 plain and 2/2 twill, also called diamond and regular pattern, respectively. The patterns are shown in Fig. 2. The angle α between the warp or weft yarn direction and the projection of mandrel centerline on the mandrel surface is defined as the braid angle.

The moving mandrel pulls the warp and weft yarns from the rotating bias spools. Each of the carriers has a tensioning mechanism to compensate for yarn length fluctuations due to the change in radial spool position. The location where a yarn first touches the mandrel is defined as the fell point. The set of the fell points, the so-called 'fell front', is circular shape in case of cylindrical mandrels and a non-circular shape in case of non-axisymmetric mandrels. A guide ring can be used to enhance control of the fiber deposition. As shown in Fig. 1(top), the distance from the fell point to the guide ring or the spool circle is defined as the length of the so-called convergence zone H. When the braid is formed on the mandrel surface, that distance is referred to as

* Corresponding authors.
E-mail addresses: a.n.vu@utwente.nl (A.N. Vu), r.akkerman@utwente.nl (R. Akkerman).

https://doi.org/10.1016/j.compositesa.2022.107421
Received 4 July 2022; Received in revised form 22 November 2022; Accepted 30 December 2022
Available online 7 January 2023

Nomenclature

Vectors:

$\mathbf{F}^{c}$	yarn–yarn contact force vector
$\mathbf{F}^{int}$	internal force vector
$\mathbf{F}^{ext}$	external force vector
$\mathbf{F}^{t}$	tangent force vector
$\mathbf{F}^{n}$	normal force vector
$\mathbf{F}_{r}$	yarn–ring contact force vector
$\mathbf{X}$	array of forces in warp yarns
$\mathbf{O}$	array of forces in weft yarns
$\mathbf{C}$	array of contact point coordinates
$\mathbf{u}$	unit yarn segment direction

Scalars:

v	take-up speed
ω	spool angular velocity
L	braided length
H	convergence zone length
α	braid angle
P_m	perimeter of mandrel cross-section
μ_y	yarn–yarn coefficient of friction
μ_r	yarn–ring coefficient of friction
θ	Eulerian degree of freedom
η	Capstan angle
f	yarn tension
r_{gr}	radius of guide ring
r_s	radius of spool circle
w_n	yarn width
t_n	yarn thickness
γ	projection angle at contact point
λ	optimal damping factor
h	frontal iteration number
ε	convergence criterion
M_{int}	initial mandrel position

Index notations:

$(*)^{m}$	warp segment number
$(*)^{n}$	weft segment number
$(*)_{i}$	warp yarn number
$(*)_{j}$	weft yarn number
$(*)^{k}$	counter number of contact row
$(*)^{K}$	total number of contact row

Operators:

$(*)^{T}$	transpose of a quantity
$\|*\|$	Euclidean norm
$(*)^{T}.(*)$	scalar product

Others:

Ψ	slipping function
n, **t**, **p**	Eulerian coordinate system
i, **j**, **k**	ring coordinate system
$(*)_{O}$	weft
$(*)_{X}$	warp

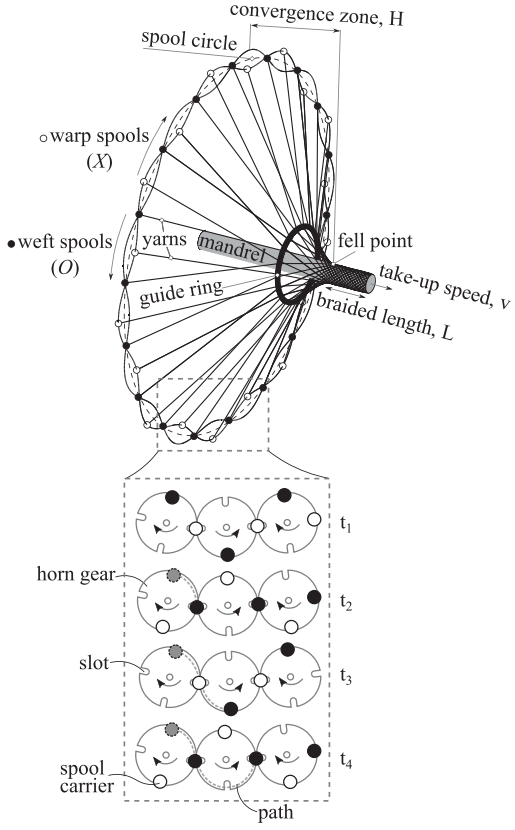

Fig. 1. Biaxial overbraiding process (top) and the spool movement for the regular pattern (bottom) for each time step.

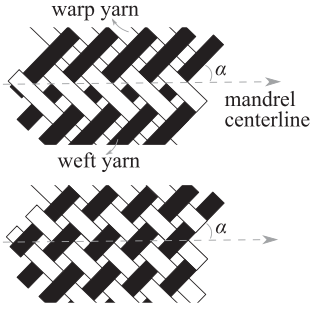

Fig. 2. Braid patterns: regular pattern (top) and diamond pattern (bottom).

the braided length L. The process usually evolves from an unsteady state to a steady state. In the steady state, the braid angle α and the convergence zone length H at a certain position along the length of the mandrel is unchanged and defined as:

$$\frac{\partial \alpha}{\partial L} = \frac{\partial H}{\partial L} = 0. \tag{1}$$

1.2. State-of-the-art

Product development can be both expensive and time-consuming as the overbraiding and infusion processes need several iterations until the design requirements are met. Predictive simulation tools for the overbraiding process can reduce the time and costs associated with product development. Several approaches are available, ranging from simple analytical models to computational expensive finite element approaches. This section briefly compares the different methods.

The overbraiding process can be modeled by analytical formulas. Ko [9] introduced a closed-form equation to calculate the braid angle

α for an axisymmetric process:

$$\alpha = \arctan\left(\frac{P_m \omega}{2\pi v}\right), \tag{2}$$

where P_m is the perimeter of the mandrel cross-section, ω is the angular velocity of the spool in radians per second, and v is the mandrel take-up speed. Kessels et al. [10] proposed an extended two-dimensional solution as a function of an eccentric variable to predict the braid angle for a non-axisymmetric process. The analytical models are fast computation times but are inaccurate because effects such as yarn interaction and tension forces from the spool carriers are ignored.

A commonly used method to model the process is by means of Finite Element (FE) simulations. Pickett et al. [11] presented an entire simulation chain using the explicit FE method. Recently, numerous studies used the FE approach to simulate the overbraiding process as described in Refs. [12–17]. FE simulations allow a detailed description of complex geometries, while also providing the flexibility to include yarn interactions, guide ring friction, yarn tensioning and bending, yarn slippage, and discontinuous yarn deposition. However, such models involve very high computational cost due to their complexity, which is usually prohibitive for conventional production development and possible optimization schemes.

The overbraiding process can also be simulated using the so-called kinematic approach suggested by Kessels et al. [10] and Monnot et al. [18]. This approach excludes the interaction between yarns as well as yarn deformation. The model offers fast computation for complex geometries. However, it comes at the cost of a decreased accuracy due to the omission of yarn interaction [19,20]. Later, van Ravenhorst et al. [21] introduced a yarn interaction model on the basis of the kinematic model. Their model considered an axisymmetric biaxial process with a cylindrical mandrel, while Coulomb's friction law was used to describe the contact between yarns. The study of Ravenhorst showed a decrease of 25% of the convergence zone length when including friction. Zhang et al. [22,23] also simulated the axisymmetrical braiding process including yarn interaction. The frictional behavior was modeled using Howell friction [6]. The friction force was obtained by solving force equilibrium in the transformed 2D plane. The comparison with experimental data showed that the model including yarn interaction had better agreement than the kinematic model. However, those studies are restricted only to an axisymmetric process, using cylindrical mandrel and excluding the use of the guide ring.

The coefficient of friction is used as an input of the model when considering yarn interaction. Several studies [24–27] reported the coefficient of friction in the range of 0.15–0.4. The coefficient of friction shows a high dependence on the normal applied force [28,29] and the angle between yarns [27,30].

1.3. Research objective

Previously, simulations of the overbraiding process have been developed using a kinematic model which offers short computational times [10]. However, these approaches neglect the yarn interactions, causing systematic deviations between the model results and the experimental data [19]. Therefore, the objective of the current work is to develop a model that includes yarn interactions for arbitrary geometries, not restricted to axisymmetric conditions [21]. We propose an improved yarn interaction model to simulate the overbraiding process for non-axisymmetric preforms. This model includes the stick–slip effect at interlaced points and the use of a guide ring. The improvements and adaptions to the model of van Ravenhorst et al. [21] are discussed. The description of the model is followed by a validation against experiments, numerical studies to demonstrate the performance of the proposed approach, and a discussion of the results.

2. Theory

In the following of this section, the model assumptions, a single yarn-to-yarn and a yarn-to-ring contact point model will be presented. Further, we will elaborate how these models are extended to account for multiple contact points.

2.1. Model assumptions

The models are described for an arbitrary braiding machine configuration. This study considers only circular spool rings. It is assumed that the mandrel and guide ring surface are completely rigid. Note that the mandrel axis is not necessary collinear with the machine axis. Yarns are considered as inextensible, straight-line segments. Only axial forces can be transferred while bending, shearing, as well as torsion, are not supported. Yarn and mandrel weight are neglected, allowing the effects of inertia to be excluded. The yarns are assumed to fully stick to the mandrel once they are in contact, excluding any slipping after deposited. Such conditions are pronated by the interlaced pattern of the braids [31]. The yarn segments are assumed to be permanently under tension, implying that their directions are collinear with the force directions. When a guide ring is used, the contacts between the ring and yarns are assumed to be point contacts.

2.2. Single yarn-to-yarn interaction model

This section presents a 3D model considering a single contact point between two yarn segments. The objective of the model is to determine the position of the contact point for any boundary condition. Fig. 3a illustrates a warp (X) and a weft (O) yarn in contact at point $\mathbf{C}$. The yarn positions are prescribed at $\mathbf{A}_X$ and $\mathbf{A}_O$, respectively. There are two external forces acting at the opposing yarn segment ends, $\mathbf{B}_X$ and $\mathbf{B}_O$. The interaction point $\mathbf{C}$ can be one of the interlaced points within the convergence zone. The points $\mathbf{A}_X$ and $\mathbf{A}_O$ are imposed by other lower interlacement points or by the fell points in case the considered interaction point is closest to the mandrel.

The position of the interlacement point is found by solving force equilibrium at the contact point. Force equilibrium must be satisfied for every cutting segment of the yarns, as illustrated in Fig. 3b. At contact point $\mathbf{C}$, the contact force can be derived as:

$$\mathbf{F}_X^c = \mathbf{F}_X^{int} + \mathbf{F}_X^{ext}, \quad \mathbf{F}_O^c = \mathbf{F}_O^{int} + \mathbf{F}_O^{ext} \tag{3}$$

where $\mathbf{F}_X^{int}$ and $\mathbf{F}_O^{int}$ are so-called internal forces and $\mathbf{F}_X^{ext}$ and $\mathbf{F}_O^{ext}$ are external forces. In addition, the contact forces must be equal with opposite directions,

$$\mathbf{F}_X^c + \mathbf{F}_O^c = \mathbf{0} \tag{4}$$

with $\mathbf{F}_X^c$ and $\mathbf{F}_O^c$ the contact forces acting from warp to weft and from weft to warp yarn, respectively. Because the positions of the points $\mathbf{A}_X$ and $\mathbf{A}_O$ are known, a vector that goes through these points can be determined, denoted as the rotational vector $\mathbf{e}_1$, shown in Fig. 3a. Since the two yarns are making contact at point $\mathbf{C}$ and assumed to be in tension, the yarn segments $\mathbf{CA}_X$ and $\mathbf{CA}_O$ can momentarily rotate around the axis $\mathbf{e}_1$. From Eqs. (3) and (4), the total internal force $\mathbf{F}_X^{int} + \mathbf{F}_O^{int}$ and total external force $\mathbf{F}_X^{ext} + \mathbf{F}_O^{ext}$ must be in the same plane and in opposite direction. As the yarn segments $\mathbf{CA}_X$ and $\mathbf{CA}_O$ are collinear with the internal forces $\mathbf{F}_X^{int}$ and $\mathbf{F}_O^{int}$, respectively, these segments rotate around the axis $\mathbf{e}_1$ and stay in the plane created by the two vectors $\mathbf{e}_1$ and $\mathbf{F}_X^{ext} + \mathbf{F}_O^{ext}$.

The constitutive equations for friction at the contact point are formulated using Amonton's friction [32]:

$$\Psi_s = \left\|\mathbf{F}^t\right\| - \mu_y \left\|\mathbf{F}^n\right\| \quad \text{and} \quad \Psi_s \begin{cases} < 0, & \text{during sticking} \\ = 0, & \text{during slipping} \end{cases} \tag{5}$$

with $\mathbf{F}^t$ and $\mathbf{F}^n$ as the tangent and normal force components of the contact force, respectively. Amonton's friction law defines a maximum

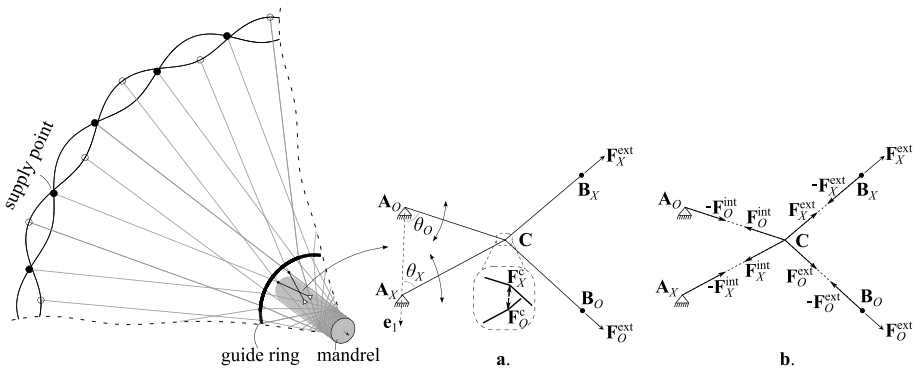

Fig. 3. Illustration of single interaction point within the convergence zone. **a**. Single contact point model. **b**. Force equilibrium at the cutting segments of the yarns.

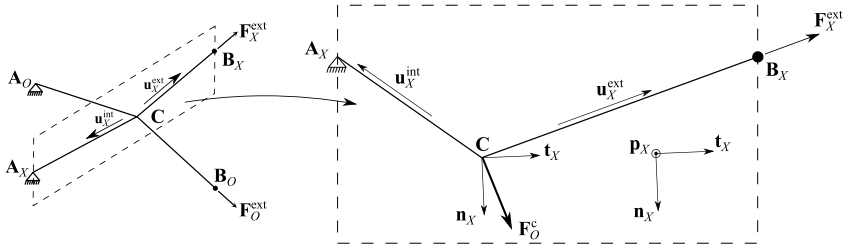

Fig. 4. Definition of Eulerian coordinate system in the warp yarn viewed perpendicularly to the warp yarn plane defined by $\mathbf{u}_X^{\text{int}}$ and $\mathbf{u}_X^{\text{ext}}$.

friction force $\mathrm{F}_{\max}^{\mathrm{t}} = \mu_{\mathrm{y}} \|\mathbf{F}^{\mathrm{n}}\|$ where μ_{y} is the coefficient of friction acting as a constant of proportionality. Obviously, in the case of sticking, the tangent force has to be smaller than the maximum friction force. Otherwise, the yarn is slipping. An Eulerian on Lagrangian approach is used, allowing the stick and slip process to be resolved. Two more Eulerian degrees of freedom, θ_O and θ_X (Fig. 3a), are added, in order to be able to account for the slipping process. The variation of the angle θ_O corresponds to the slipping of the weft yarn over the warp yarn, while the opposite holds for the angle θ_X. The angles θ_O and θ_X are fixed in the case of stick, while they vary when slipping.

Fig. 4 represents the interaction in the plane of the warp yarn segments, with unit vectors $\mathbf{n}_X$ and $\mathbf{t}_X$ lying on this plane and unit vector $\mathbf{p}_X$ normal to this plane. The Eulerian coordinate system is defined as:

$$\mathbf{n}_X = -\frac{\mathbf{u}_X^{\text{int}} + \mathbf{u}_X^{\text{ext}}}{\left\|\mathbf{u}_X^{\text{int}} + \mathbf{u}_X^{\text{ext}}\right\|} \quad \text{and} \quad \mathbf{n}_X \perp \mathbf{t}_X \perp \mathbf{p}_X. \tag{6}$$

Here, the tangent vector $\mathbf{t}_X$ points to the direction of motion. The force $\mathbf{F}_O^{\mathrm{c}}$ acts as an external force on the weft yarn while the warp yarn is the reference for the sliding direction. Because the total contact force $\mathbf{F}_O^{\mathrm{c}}$ always lies in the same plane with $\mathbf{n}_X$ and $\mathbf{t}_X$, it can be decomposed into tangential and normal contributions using this coordinate system:

$$\mathbf{F}_O^{\mathrm{n}} = \mathbf{n}_X.(\mathbf{F}_O^{\mathrm{c}})^{\top}.\mathbf{n}_X \quad \text{and} \quad \mathbf{F}_O^{\mathrm{t}} = \mathbf{t}_X.(\mathbf{F}_O^{\mathrm{c}})^{\top}.\mathbf{t}_X. \tag{7}$$

From Eqs. (5) and (7), a slipping criterion, $\Psi_{\mathrm{s}}(\theta_O)$, for the weft yarn is derived. Similarly, equation $\Psi_{\mathrm{s}}(\theta_X)$ can be found for the warp yarn. The system of equations is solved for θ_O and θ_X when reaching the slipping conditions as indicated in Eq. (5):

$$\begin{aligned} \Psi_{\mathrm{s}}(\theta_O) &= \left\|\mathbf{F}_O^{\mathrm{t}}(\theta_O)\right\| - \mu_{\mathrm{y}} \left\|\mathbf{F}_O^{\mathrm{n}}(\theta_O)\right\| = 0, \\ \Psi_{\mathrm{s}}(\theta_X) &= \left\|\mathbf{F}_X^{\mathrm{t}}(\theta_X)\right\| - \mu_{\mathrm{y}} \left\|\mathbf{F}_X^{\mathrm{n}}(\theta_X)\right\| = 0. \end{aligned} \tag{8}$$

Three slipping cases are distinguished as shown in Fig. 5. A predictor–corrector algorithm is implemented for these cases as illustrated in Fig. 6. In case 1, the weft yarn starts to slip when $\Psi_{\mathrm{s}}(\theta_O) > 0$. The equation $\Psi_{\mathrm{s}}(\theta_O) = 0$ is solved to obtain the new value of θ_O. Since the warp yarn is sticking or $\Psi_{\mathrm{s}}(\theta_X) < 0$, the value of θ_X remains unchanged. A similar solving process is applied to case 2. In both cases, the solution of θ_O or θ_X of the slipping yarn can be obtained analytically. In case 3, both yarns are slipping. A system of two nonlinear equations of Eq. (8) has to be solved. Since it is hardly feasible to solve this system of equations analytically, an iterative procedure is applied to obtain the solutions. The procedure starts with solving case 1 to obtain the new θ_O. Next, case 2 is solved for the new θ_X while θ_O is fixed. The procedure is repeated until a small change of $\Psi_{\mathrm{s}}(\theta_O)$ and $\Psi_{\mathrm{s}}(\theta_X)$ are achieved.

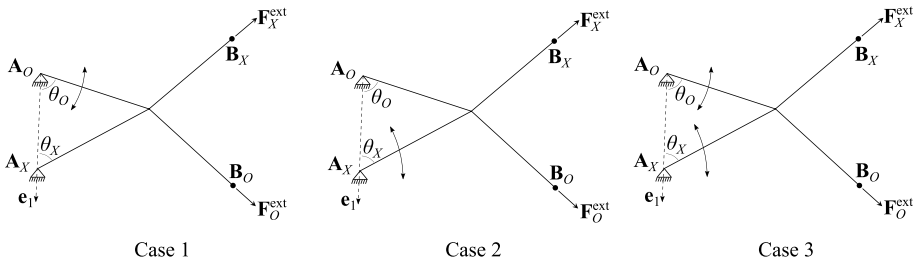

Fig. 5. Slipping cases. Case (1) weft yarn in slip, warp yarn in stick. Case (2) warp yarn in slip, weft yarn in stick. Case (3) both yarns in slip.

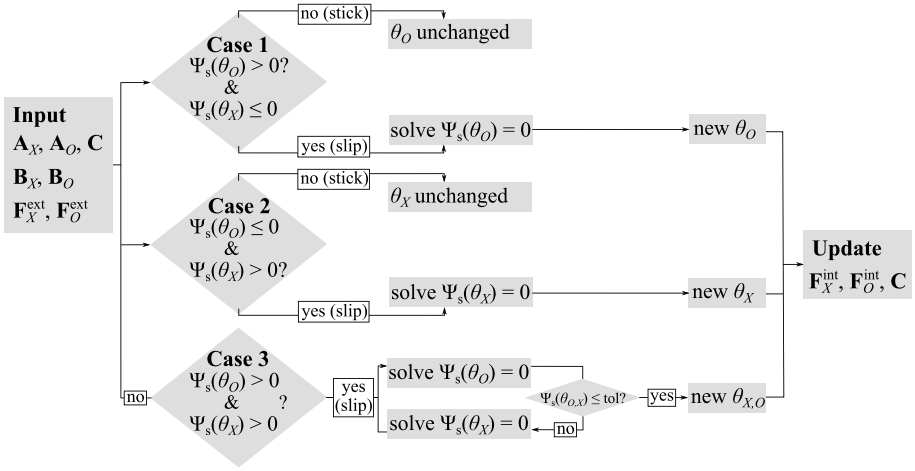

Fig. 6. Flowchart of the predictor–corrector algorithm of the single yarn-to-yarn contact point model.

2.3. Yarn and guide ring contact model

This section presents an interaction model between a yarn and the guide ring as illustrated in Fig. 7. The ring is assumed to be circular with given radius r_{gr}. The yarn's end point position **A** is prescribed while the fiber tension $\mathbf{F}_r^{ext}$ is prescribed at the end point **B**. The yarn can be one of the segments from an interlacement point, wrapping around the guide ring to the supply point as shown in Fig. 7. The fixed point **A** is imposed by the position of the last interlaced point of the braid, while the external force $\mathbf{F}_r^{ext}$ can be applied from the supply point.

The position of the contact point **R** on the guide ring can be described in terms of the angle θ_r, defined in the local ring coordinate system (**i**, **j**, **k**). For an arbitrary boundary condition, the yarn can slip over the guide ring in longitudinal and transverse directions. The line contact of the yarn wrapping over a cylindrical cross-section of the guide ring is simplified to a point contact as point **R**. The Capstan relation [24,27] is used to model the longitudinal forces:

$$f_{ext} = f_{int} e^{\eta \mu_r}, \tag{9}$$

where f_{int} and f_{ext} are tension forces in the yarn ends **A** and **B**, respectively, μ_r is the yarn-to-ring coefficient of friction and η is the Capstan angle of the yarn wrapping the ring. Each time step, the variation of the Capstan angle can be computed as the angle between the normal unit vectors of the yarn two yarn segments **AR** and **BR**. The total of the two force vectors, $\mathbf{F}_r^{int}$ and $\mathbf{F}_r^{ext}$ results in the contact force at the contact point as illustrated in Fig. 7b:

$$\mathbf{F}_r = \mathbf{F}_r^{int} + \mathbf{F}_r^{ext}, \tag{10}$$

here, the internal force vector $\mathbf{F}_r^{int} = f_{int}\mathbf{u}_r^{int}$ can be calculated by the unit vector $\mathbf{u}_r^{int}$ and the axial force f_{int} from Eq. (9). Similarly to the yarn-to-yarn contact model, the friction in the transverse direction is modeled using the Eulerian on Lagrangian method. The stick and slip process is captured using Amonton's friction. The slipping criterion for the transverse direction can be written as:

$$\Psi_r(\theta_r) = \left\|\mathbf{F}_r^t\right\| - \mu_r \left\|\mathbf{F}_r^n\right\| \quad \text{and} \quad \Psi_r \begin{cases} < 0, & \text{during sticking} \\ = 0, & \text{during slipping} \end{cases} \tag{11}$$

here, the Eulerian degree of freedom θ_r is introduced to enable the slipping process of the yarn in the transverse direction. The tangential and normal force components of the contact force can be calculated by:

$$\mathbf{F}_r^t = \mathbf{t}_r.(\mathbf{F}_r)^T.\mathbf{t}_r \quad \text{and} \quad \mathbf{F}_r^n = \mathbf{n}_r.(\mathbf{F}_r)^T.\mathbf{n}_r \quad \text{and} \quad \mathbf{n}_r \perp \mathbf{t}_r. \tag{12}$$

The tangent vector $\mathbf{t}_r$ and normal vector $\mathbf{n}_r$ are unit vectors as demonstrated in Fig. 7. The vector $\mathbf{t}_r$ is tangent to the guide ring curvature and derived in the ring coordinate system as:

$$\mathbf{t}_r = r_{gr} \begin{bmatrix} -\sin\theta_r \\ \cos\theta_r \\ 0 \end{bmatrix} \tag{13}$$

with r_{gr} the guiding ring radius. The normal vector $\mathbf{n}_r$ lies in the plane containing the contact force $\mathbf{F}_r$ and the tangent vector $\mathbf{t}_r$. Eqs. (9), (10), (12), (13) are used in conjunction with the slip criterion Eq. (11) to check the stick–slip condition. A predictor–corrector algorithm as shown in Fig. A.17 is used to account for the stick–slip process. In the case of slip, the new position of the contact point **R** on the ring needs to be determined. Since the position of point **R** can be described by the angle θ_r, the slipping condition $\Psi_r(\theta_r) = 0$ in Eq. (11) can be solved to find θ_r instead. The unknown θ_r is unchanged in the case of sticking.

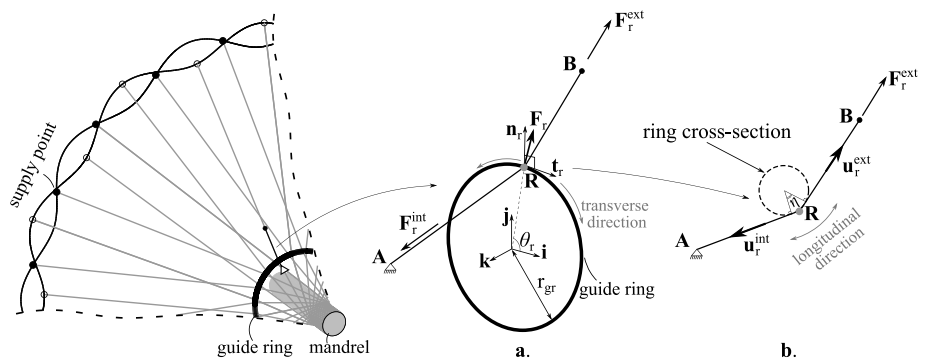

Fig. 7. Yarn and ring interaction model. **a**. Ring cross section viewed perpendicularly to the tangent vector $\mathbf{t}_r$ showing Capstan angle η, **b**. Details of yarn and ring contact model in the transverse direction.

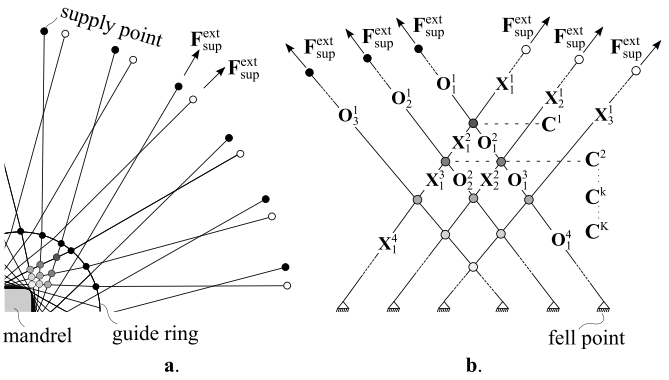

Fig. 8. Multiple contact points model. **a**. Front view of biaxial overbraiding mode with yarn interlacements. **b**. Definition of row contact and axial forces in the frontal approach procedure. The force vectors $\mathbf{X}_i^m$, $\mathbf{O}_j^n$ and the contact coordinate vectors $\mathbf{C}^k$ denoted as bold symbols.

2.4. Frontal solver for multiple contact points model

By applying the above single contact point models, we were able to develop a model for multiple contact points which can be used for a non-axisymmetric overbraiding process with a guide ring.

2.4.1. Frontal procedure

A multiple contact points problem needs to be solved when the yarns are fully interlaced at the convergence zone. The problem usually consists of a large number of highly non-linear equations in which the contact positions and resultant forces are the unknowns. A non-linear iterative solver can be used, however, this solver has the time complexity of $\mathcal{O}(n^3)$ for n unknowns [21]. Van Ravenhorst et al. [21] proposed a computational method, a so-called frontal approach, sweeping a single contact point at a time from the fell points to the supply points, offering a very fast computational time with an $\mathcal{O}(n)$ time complexity. This approach was extended for our multiple contact points model, which will be further discussed in details below.

Assuming that the fell points stick completely on the mandrel after making contact, the coordinates of these points are always known. Fig. 8a shows a front view of a biaxial overbraiding process, while Fig. 8b shows the corresponding group of interlaced weft and warp yarns. The yarns are divided into segments by the contact points. Starting from the supply points and moving to the fell points, rows of contact points are defined as gray color coded. The last row indicates the fell points. The force vector of each yarn segment is introduced in index notation as $\mathbf{X}_i^m$ and $\mathbf{O}_j^n$ for warp and weft yarn, respectively. The subscript i and j refer to warp and weft yarn numbers, respectively. The yarn segment numbers are denoted by the superscript m and n. The vector containing contact coordinates of each row is denoted using index notation as $\mathbf{C}_j^k$, where the index k is the row number. The contact point number in each row is counted using the weft yarn number j.

In the proposed approach, the boundary conditions are the positions at the fell points and the spool tension $\mathbf{F}_{sup}^{ext}$ applied at each supply point. In contrast to the algorithm proposed by Van Ravenhorst et al. [21], the current simulation uses a two-step scanning procedure. First, from the supply points progressing through the interlaced points to the fell points, the magnitude and direction of the force components are calculated. Second, from the fell points to the supply points, the positions of the intermediate contact points are determined using the calculated forces.

From the first interlaced row $\mathbf{C}^1$, by considering the points of the second row $\mathbf{C}^2$, as virtual fixed points, the single contact solver is executed at every point of the $\mathbf{C}^1$ row to obtain the internal forces of the next yarn segments. These forces are treated as the external forces for the following row. The process continues until reaching the fell points, enabling to obtain the force vectors, $\mathbf{X}_i^m$ and $\mathbf{O}_j^n$, of all yarn segments. The corresponding unit vectors of the yarn segments can be derived as:

$$\mathbf{u}_{X,i}^m = \frac{\mathbf{X}_i^m}{\left\|\mathbf{X}_i^m\right\|} \quad \text{and} \quad \mathbf{u}_{O,j}^n = \frac{\mathbf{O}_j^n}{\left\|\mathbf{O}_j^n\right\|}. \tag{14}$$

Clearly, the positions at the fell points are known, allowing to update the coordinates of the contact points in row k − 1 using a parametric equation:

$$\mathbf{C}_j^{k-1} = \mathbf{C}_j^k + p_k.\mathbf{u}_{O,j}^n. \tag{15}$$

The contact point coordinates can be calculated using the weft yarn directions $\mathbf{u}_{O,j}^n$ of the corresponding segments n. The parameter p_k can be found by solving the problem of the two intersected lines. A similar method was used in Ref. [21] where the p_k was the length of the yarn segment. The determined positions are then used as the boundary conditions for calculating the position of the contact points in the next $\mathbf{C}^{k-2}$ row. This process is repeated until all positions of the contact points are determined.

2.4.2. Yarn thickness

Yarn thickness plays a crucial role in the undulation of the braid structure. It is also the reason for inducing the contact forces at the intermediate points. The yarn shape is modeled as a rectangular cross-section with a width w_n and a thickness t_n. The yarn width can be modeled as a function of the available width as in Ref. [21]. The model enables the yarn width to be reduced without deformation resistance while the spreading of the yarn is not affected by the contact force. Fig. 9a illustrates a diamond braid pattern including the thickness. The dashed line represents the centerline of the yarn, whereas the solid line indicates the contact interface of two interlaced yarns. An axial force must be parallel to the yarn centerline. In Fig. 9, the contact interface is represented as the dot symbols, the so-called true contact points.

In order to determine the position of the contact point $\mathbf{C}^{k-1}$ within the row k − 1 (see Fig. 9a), the two points $\mathbf{C}_X^k$ and $\mathbf{C}_O^k$ will be treated as virtual fixed points. Taking into account the effect of the yarns' thickness, the two virtual fixed points are shifted to $\mathbf{A}_X$ and $\mathbf{A}_O$, respectively, by means of:

$$\begin{aligned}\mathbf{A}_X &= \mathbf{C}_X^k + \frac{\mathbf{n}_X^k \cdot t_n}{2 \cdot \cos(\gamma_X^k)} - \frac{\mathbf{n}_X^{k-1} \cdot t_n}{2 \cdot \cos(\gamma_X^{k-1})} \\ \mathbf{A}_O &= \mathbf{C}_O^k + \frac{\mathbf{n}_O^k \cdot t_n}{2 \cdot \cos(\gamma_O^k)} - \frac{\mathbf{n}_O^{k-1} \cdot t_n}{2 \cdot \cos(\gamma_O^{k-1})}\end{aligned} \tag{16}$$

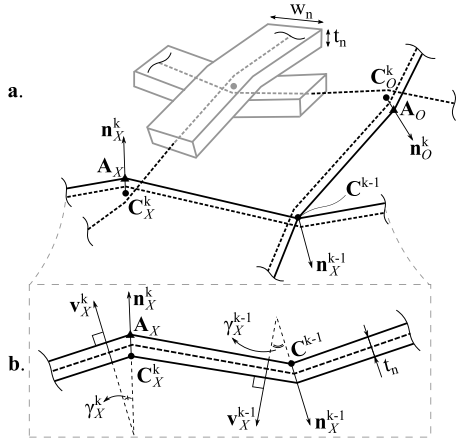

Fig. 9. Model of yarn thickness considering rectangular cross-section of the yarn for the diamond braid pattern. **a**. The shift thickness direction from real contact points to the virtual fix points. **b**. Cross-section of yarn viewed perpendicularly to its centerline.

where $\cos(\gamma_{X,O}^{k,k-1}) = (\mathbf{n}_{X,O}^{k,k-1})^{\mathsf{T}} \cdot \mathbf{v}_{X,O}^{k,k-1}$ are the projections of the thickness onto the normal referenced directions, as illustrated in Fig. 9b. The combination of the consecutive normal references guaranty a consistency in forces and nodal coordinate results.

2.4.3. Iterative treatments

Force equilibrium, Eq. (3), and slipping conditions Eq. (5) must be fulfilled at each interlacement point for the multiple contact points case. The frontal approach using one time two-step scanning, as described above, does not provide solutions with sufficient accuracy. For example, the solution of the upper row(s) will not hold true anymore when external forces cause the slipping of more than one row. Multiple times two-step scanning results in numerical instabilities.

To overcome the problem, we used a linear iterative method, particularly called the minimum residual method, to approximate the solutions. For each iteration, the frontal approach is called to update the positions of the contact points. In the next iteration, the positions of the contact points are updated using the solutions of the previous iteration as:

$$\mathbf{C}_{h+1} = \mathbf{C}_h + \lambda \mathbf{r}_{h-1} \quad \text{where} \quad \lambda = \frac{(\mathbf{r}_{h-2})^{\mathsf{T}}.\mathbf{r}_{h-2}}{(\mathbf{r}_{h-1})^{\mathsf{T}}.\mathbf{r}_{h-1}}, \tag{17}$$

with $\mathbf{r}_{h-2} = \mathbf{C}_{h-2} - \mathbf{C}_h$ and $\mathbf{r}_{h-1} = \mathbf{C}_{h-1} - \mathbf{C}_h$ being respectively the differences of the contact positions between iterations, λ an optimal damping factor, and h = 1, 2, 3... the iteration number. Here, the bold $\mathbf{C}$ indicates an array containing all of the contact point coordinates. It is noted that $\mathbf{C}_{h-1} = \mathbf{C}_{h-2}$ at the first iteration h = 1. The array $\mathbf{C}_{h+1}$ contains the initial contact point positions at the starting of an iteration h+1 and $\mathbf{C}_h$ is the calculated positions at the end of iteration h using the frontal approach. Eq. (17) was updated by minimizing the residual $\mathbf{r}_{h-3} = \mathbf{r}_{h-2} + \lambda \mathbf{r}_{h-1}$. This means that the damping factor λ was determined such that the function $f(\lambda) = \|\mathbf{r}_{h-2} + \lambda \mathbf{r}_{h-1}\|^2$ is at minimum. With a high number of rows, a more efficient stabilized treatment can be used by gradually increasing the number of rows in consideration with a step size of h_{step}. The computational process is continued until reaching the fell points. The procedure stops when a noticeably low alteration of the position is satisfied with the convergence criterion ε.

2.5. Implementation

At the supply points, the new row of the contact points is formed continuously using a contact detector among the yarns. Similarly, the fell points are relocated whenever the last row of contact points is in contact with the mandrel. In case the guide ring is used, the frontal procedure starts from the guide ring to the fell points. The full algorithm was implemented with the iterative frontal approach as shown in Fig. 10. The algorithm shows linear convergence with the number of iterations (see Fig. B.18). The computational time is approximately proportional to the number of contact points and lies in the order of minutes for a full simulation even for a large number of contact points with the current MATLAB® implementation.

After completing a simulation, a post-processing procedure was utilized to estimate the braid angle on the mandrel surface. The same definition of braid angle was used by others [10,19,31]. At each interlaced point, the braid angle is calculated as the angle between the direction of the weft or warp yarn segment and the projection of the mandrel centerline tangent on the mandrel surface.

3. Experimental and numerical case study

3.1. Experimental validation

The presented model was validated against previous experimental data for an axisymmetric case from Ref. [21] (case A) and a non-axisymmetric case from Ref. [10] (case B). The experiments were performed at EuroCarbon B.V. in the Netherlands. The two mandrel

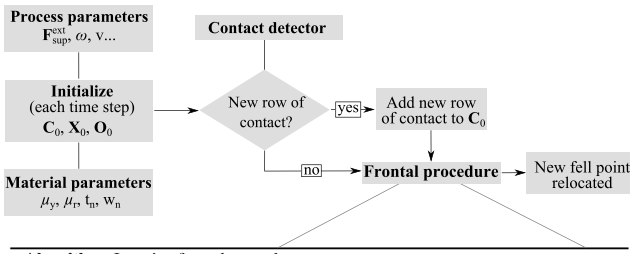

Algorithm: Iterative frontal procedure

Input : $\mathbf{C}_0, \mathbf{X}_0, \mathbf{O}_0$

Objective: $\|\Delta\mathbf{C}\| < \varepsilon, \Psi_s \leq 0, \Psi_r \leq 0$

Initialization *integer* h_{step};

▷ loop over the row until reaching end row K

for $k = 1;\ k < K;\ k = k + h_{step}$ **do**

  $h \leftarrow 0$

  do

    $h \leftarrow h + 1$

    ▷ Swept from supply points to row k

    for $k' = 0;\ k' \leq k;\ k' = k' + 1$ **do**

      ▷ Each contact point

      Update yarn thickness using (16)

      Solve the single contact point problem using flowchart Figure 6 ($k' \geq 1$) or Figure A.17 ($k' = 0$)

      Update the force vector $(\mathbf{X}_i^m)_h$ and $(\mathbf{O}_j^n)_h$ of yarn segments

    end

    ▷ Assign previous contact coordinates

    $\mathbf{C}_{h-2} \leftarrow \mathbf{C}_{h-1}$

    $\mathbf{C}_{h-1} \leftarrow \mathbf{C}_h$

    ▷ Swept from row k to supply points

    for $k' = k;\ k' \geq 1;\ k' = k' - 1$ **do**

      ▷ Each contact point

      Update the contact coordinates $\mathbf{C}_h$ using (14) and (15)

    end

    $\mathbf{r}_{h-2} \leftarrow \mathbf{C}_{h-2} - \mathbf{C}_h$

    $\mathbf{r}_{h-1} \leftarrow \mathbf{C}_{h-1} - \mathbf{C}_h$

    $\lambda \leftarrow \frac{(\mathbf{r}_{h-2})^{\mathsf{T}}.\mathbf{r}_{h-2}}{(\mathbf{r}_{h-1})^{\mathsf{T}}.\mathbf{r}_{h-1}}$

    $\mathbf{C}_{h+1} \leftarrow \mathbf{C}_h + \lambda \mathbf{r}_{h-1}$

  while $(\|\mathbf{r}_{h-1}\| > \varepsilon)$;

end

Fig. 10. Flowchart of the full implementation including the algorithm of the frontal procedure.

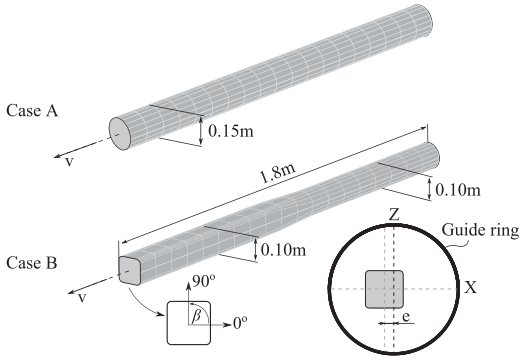

Fig. 11. Mandrels for axisymmetric (case A) and non-axisymmetric (case B) process, with dimensions. Mandrel in case B clamped with an eccentricity e in the X-direction of the guide ring.

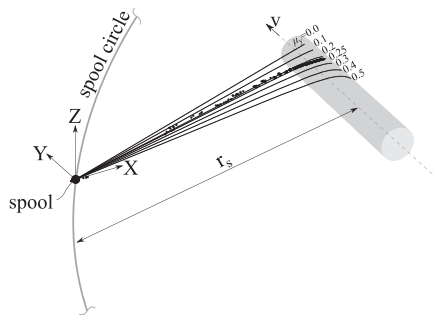

Fig. 12. Experimental and simulation results for the case A. Yarn coordinates from the experiment (dots) and simulations (line) plotted from the fell points to the same spool position for different coefficients of friction μ_y. The results was exported at the steady state and the origin was moved to the spool position.

geometries are shown in Fig. 11. The yarn-to-yarn coefficient of friction is one of the parameter inputs necessary for the simulation validation. In this current study, an experimental setup to determine the friction coefficient between yarns is not available. Therefore, a parametric study will be performed with respect to the assumed coefficient of friction and the initial convergence zone length. In the next sections, a short summary of the experimental work is provided, followed by a description of the parametric studies using the new model.

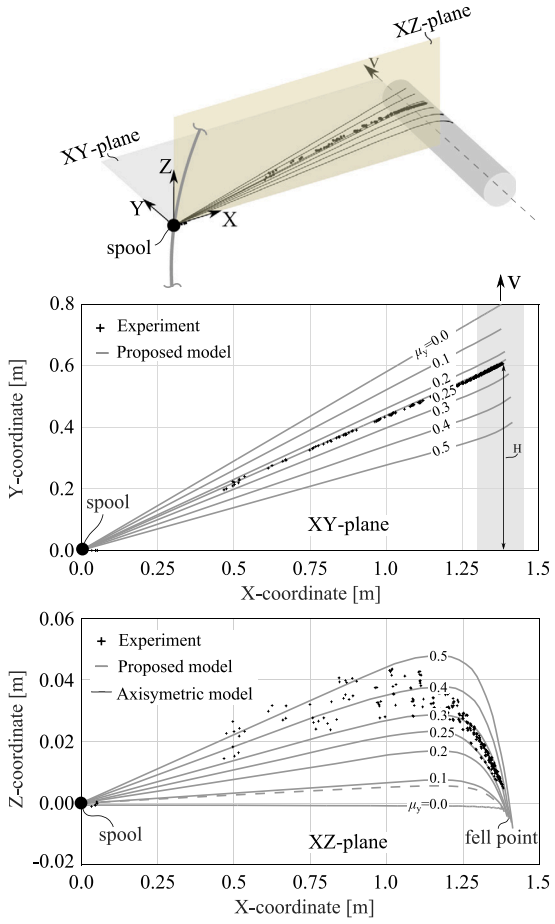

Fig. 13. Experimental and simulation results for the case A: (top) definition of projection planes, (middle) projections of experimental and simulated yarn coordinates on the XY-plane, (bottom) projections of experimental and simulated yarn coordinates from the spool on the XZ-plane. The dashed line presents yarn coordinates of the axisymmetric model with omitting the stick–slip effect [21] and $\mu_{ap} = 0.3$.

3.2. Case A: axisymmetric process

Case A concerns the overbraiding of a cylindrical mandrel. A 144-carrier overbraiding machine was utilized without a guide ring. The mandrel centerline coincided with the braiding machine axis. The same carbon fiber was used for all yarns, namely Teijin Toho Tenax IMS65 E23 24k carbon. The process reached a steady state braid angle of 60°. The trajectories of ten warp yarns were exported using Photomodeler® and used to compare with the model results. Details can be found in [21].

3.3. Case B: non-axisymmetric process

The mandrel of case B is more complex. The cross-section varies along the path from a rounded square to a circular shape. A 96-carrier overbraiding machine with a circular guide ring was utilized for this experiment starting with an initial convergence length of $H_{int} = 0.2$ m. In this case, the mandrel centerline was shifted away from the braiding machine centerline with an eccentricity of 0.025 m in X-direction, making it a non-axisymmetric process. The process had a mixture of 72 spools of 300 tex glass yarns (EC13.300.Z20.1383) and 24 spools with 110 tex polyester yarns from Danfilex. The overbraiding process started at the square cross section of the mandrel. The braided angle was determined manually using a goniometer along the four sides of the mandrel. Details can be found in [10].

3.4. Parametric study

In the case A, we performed two parametric studies using the proposed model to learn the effects of: first, the yarn-to-yarn coefficient of friction μ_y and second, the initial mandrel position M_{int} on the convergence zone length H and the braid angle α. It is noted that the initial mandrel position M_{int} is the starting distance from the mandrel tip to the spool plane. In the first study, the yarn-to-yarn coefficient of friction μ_y was varied from 0.0 to 0.5 while keeping the value of M_{int} as a constant of 0.4 m. In the second study, the effects of the initial mandrel position M_{int} was studied by varying different values of 0.2 m, 0.4 m, 0, 6 m, 0.8 m while keeping the yarn-to-yarn coefficient of friction as constant, $\mu_y = 0.3$. Table 1 shows the process parameters including the yarn properties and machine dimensions. These parameters were used consistently for all simulations. The simulations were performed until reaching the steady state when Eq. (1) was satisfied.

In the case B, we performed the simulations using the process parameters as in the experiment. The process parameters were listed in Table 1 which was kept the same for all simulations. Uniform yarn-to-yarn friction coefficients were varied between three values $\mu_y = 0.0, 0.25, 0.5$. The yarn to guide ring contact model had a friction coefficient μ_r of 0.17 as measured by Cornelissen et al. [24]. The initial convergence zone length was kept constant in this case equal to the reported experimental value $H_{int} = 0.2$ m.

Table 1
Experimental parameters for the overbraiding processes.

Parameter	Case A	Case B
Initial yarn thickness, t_n (m)	$2.5 \cdot 10^{-4}$	$2.5 \cdot 10^{-4}$
Initial yarn width, w_n (m)	$4 \cdot 10^{-3}$	$4 \cdot 10^{-3}$
Spool plane radius, r_s (m)	1.382	0.85
Guide ring radius, r_{gr} (m)	–	0.17
Spool number each group	72	48
Braid pattern	Regular	Regular
Spool tension, (N)	4.7	4.7
Take-up speed, v (m/s)	0.01	0.0263
Angular spool velocity, ω (°/s)	13.232	18

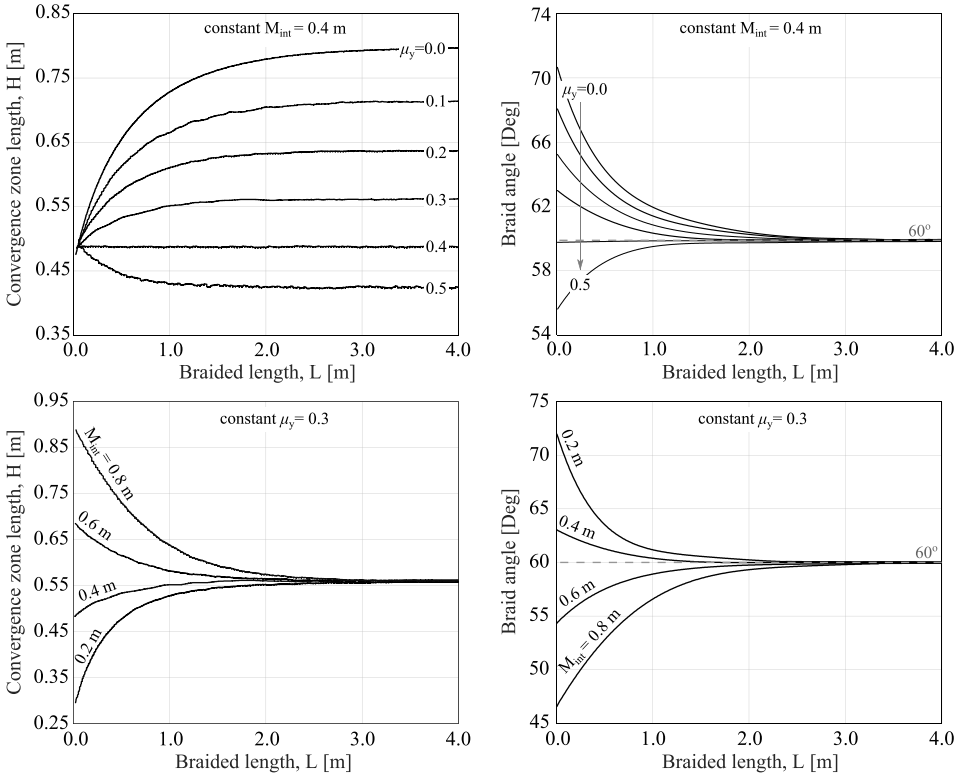

Fig. 14. Simulation results on the parametric study of case A: (top) the convergence zone length H and the corresponding braid angle as a function of the braided length L, with varying friction coefficients μ_y and constant initial mandrel position M_{int} = 0.4 m, (bottom) the convergence zone length H and the corresponding braid angle as a function of the braided length L, with varying initial position and constant yarn-to-yarn coefficient of friction μ_y = 0.3.

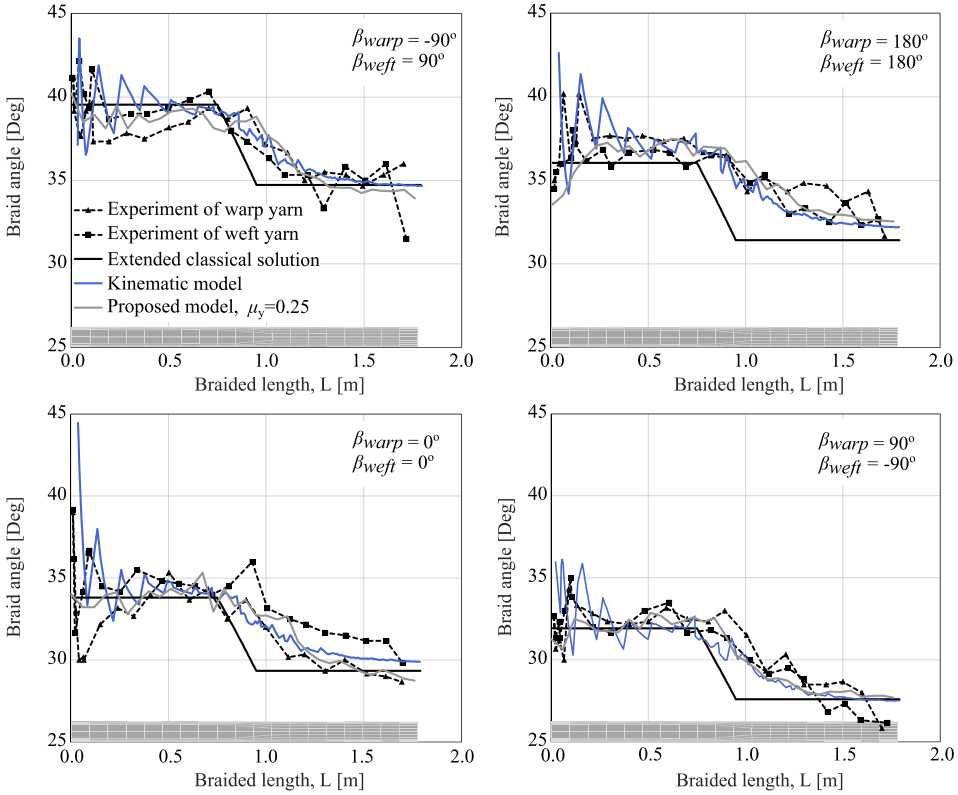

Fig. 15. Comparison of braid angle between experimental and simulation results for case B along the four sides of the mandrel using the new model, extended classical solution (analytical formulas) [10], and the kinematic model (without yarn interaction) [10]. The mandrel geometry is plotted in the bottom for reference. It shows a transition from a square to a circular cross-section at a length of 1.0 m.

4. Results and discussion

4.1. Case A

The simulated yarn curvatures were plotted against the experimental data as shown in Fig. 12. It should be mentioned that both data were exported when the process reached the steady state. The origin was moved to the spool position for comparing purpose. Fig. 13 shows the projected curves in the same planes as well as the earlier published simulation results from Ref. [21].

Fig. 13(middle) shows the projections of the experimental and calculated yarn curvatures from the spool to the fell point on the XY-plane for various values of μ_y. On this plane, the convergence zone length is the distance from the fell point to the origin in the Y-direction. For example, the distance is denoted as H in Fig. 13(middle). The results show that when the friction coefficient increases, the steady-state convergence zone length decreases. For $\mu_y = 0.25$, a very good agreement was observed between the new simulation results and the experimental curves with both of these data converging to the same convergence zone length of H = 0.622 m.

Fig. 13(bottom) shows the projections of the experimental and the simulated data on the XZ-plane. The simulation results show larger and higher curvatures near the fell point when using higher friction coefficient. The curvatures continuously decrease toward the spool at X = 0 m. This observation agreed with the trend found in the experimental results. At $\mu_y = 0.25$, the simulated curve is closest to the experimental data with an average deviation of 10 mm. Compared to the previous axisymmetric model, the new model provides results with a significant improvement in the accuracy of the findings in the XZ-plane. This can be attributed to including the stick–slip process at the contact points, which was omitted in the earlier axisymmetric model [21]. The used friction coefficient $\mu_y = 0.25$ lies in the same order of magnitude as the coefficients reported in the literature, which range from of 0.15 to 0.4 [24–27].

The effect of the friction coefficients on braid angle within the unsteady state region is shown in Fig. 14(top). The braid angle converged to the target braid angle as a result of changes in the convergence zone lengths. The new model shows that the friction coefficient has a strong effect on the braid angle within the unsteady state region, while no dependence is found after reaching steady state. The convergence zone lengths for different coefficient of frictions converged to different constant values in the steady state. The converged values of H increase with decreasing coefficients of friction.

The initial position of the mandrel also significantly affects the converging process from unsteady to steady state of the braid. As shown in Fig. 14(bottom), when varying the initial position of the mandrel using the same friction coefficient, the simulated convergence zone lengths started from considerable different values and converged to the one constant value at steady state. The corresponding braid angle was distinct at the unsteady state regime. The shorter the initial relative position of the mandrel, the larger the starting braid angle.

4.2. Case B

The predictions of the new model for case B were compared with the data from the experiment, the extended classical solution, and the kinematic model [10]. It is noted that the extended classical solution is a closed-form solution and the kinematic model excludes the interaction between yarns. The braid angles were plotted for the four sides of the mandrel similar to the results presented in [10]. The four positions were defined by a counter-clockwise angle β from the x-axis at $0, 90, -90, 180°$ (see Fig. 11). As reported in Ref. [10], the eccentricity led to the four distinct variations of braid angles and the movement of the weft and the warp spools is symmetric with respect to the XY-plane in Fig. 11(case B). The braid angle of the side β_{warp} is therefore equal to the braid angle in the side $-\beta_{weft}$ and reversely.

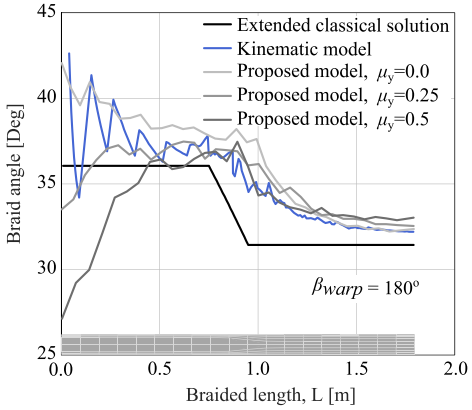

Fig. 16. Simulation results on the parametric study of case B. The warp braid angle at $\beta = 180°$ as a function of the braided length L, with varying friction coefficients μ_y using the new model. The extended classical solution (analytical formulas) and the kinematic model (without yarn interaction) [10] are included for comparison.

Fig. 15 depicts the variation of the braid angle as a function of the braided length at the four positions of the mandrel cross-section. The extended classical solution showed a stepwise decrease of the braid angle at the transition from square to circular cross-section while the experimentally measured angle changes more gradually. Note that the extended classical solution is a prediction of the braid angle rather than the targeted braid angle. The simulation data from the original kinematic model (without yarn interactions) and the new model (including yarn interactions) captured well the variations of the braid angle at the transitions of the cross-section. At this point, the two models had a maximum difference of 1.5° on average across the four positions. It is worth adding that the cross-section perimeter at this transition does not change dramatically. However, the deviations between the two models were considerable when the process was in the unsteady state (braided length from 0.0 m to 0.25 m). With $\mu_y = 0.25$, our proposed model was able to deduce a starting braid angle which was much closer to the experimental data comparing to all others models.

Fig. 16 shows the simulation results of the warp braid angle at $\beta = 180°$. The braid angle converged differently within the square cross-section region with varying the yarn-to-yarn coefficient of friction. The results confirm the effect of the coefficient of friction on the braid angle within the unsteady state regime. In case $\mu_y = 0.0$, the braid angle started with a high value and converged closely to the steady state. It ended up with the same value as other curves at the circular cross-section. With higher friction coefficients, the simulations showed a lower braid angle at the beginning. This is due to the fact that when the friction coefficient is low, the yarns have more possibilities to slip over each other toward the fell points resulting in a larger braid angle. The simulations showed a decrease of the starting braid angle of 15° with an increase of μ_y from 0 to 0.5. The extended classical solution, and the kinematic model were included for a comparison. The kinematic model without yarn interaction showed more fluctuations at the beginning. The braid angle at the unsteady state using the new model with $\mu_y = 0.5$ was much lower comparing to that of the kinematic model and the extended classical solution.

Other parametric investigations of the new model are provided in Appendix D. The results indicated that there was no significant effect with a change of the spool tension as a result of using Amonton's friction. Besides, the yarn-to-ring friction coefficient had a small effect on the braid angle and the convergence zone length in the unsteady state regime. As the yarn can wrap over the mandrel, the simplification of neglecting yarn width and ring thickness is clearly a limitation of the model. The error increases for a large yarn width and ring thickness.

5. Conclusion

A fast biaxial overbraiding model including yarn interactions for the non-axisymmetric process is developed. The stick–slip process at the cross-over point between yarns and at the yarn–ring contact is taken into account using the Eulerian on Lagrangian method. This solution is implemented in a multiple contact points model employing a fast iterative frontal approach. The validations of the new model against experimental data of axisymmetric and non-axisymmetric cases show a significant improvement of the predictions compared to earlier published simulation results. The parametric study also confirms that the interaction between yarns strongly affects the braid angle and the convergence zone length. The effects are seen within the unsteady state region for both validation cases. As observed, the initial mandrel position is a sensitive parameter to the braid angle that deserves attention when operating the process. The initial distribution of the yarns around the circumference of the mandrel tip can be random which leads to fluctuations in the braid angle at the beginning of the mandrel.

The observation indicates that the yarn interaction is important to predict the fiber distribution when the process changes from unsteady state to steady state. Examples of such situations can be a sudden change in the take-up speed, the spool angular velocity, the cross-section of the mandrel, the axis position, or in case of reversed.

For future research, the model can be extended for more complex process configurations. For example when mixing different yarn materials leading to distinct yarn contacts with individual coefficients of friction. Further, an anisotropic slipping criterion can be incorporated which further depends on contact pressure and loading speed. An experimental method should be developed to determine the coefficient of friction used as an input of the overbraiding model. Besides, the model has the potential to be extended to simulate other applications such as structural analysis of fabrics, triaxial overbraiding process with additional axial yarn group, or multiple lay-up overbraiding.

CRediT authorship contribution statement

A.N. Vu: Methodology, Software, Formal analysis, Investigation, Validation, Data curation, Visualization, Writing – original draft. **W.J.B. Grouve:** Conceptualization, Writing – review & editing, Supervision. **R. Akkerman:** Conceptualization, Resources, Writing – review & editing, Supervision, Project administration, Funding acquisition.

Declaration of competing interest

The authors declare that they have no known competing financial interests or personal relationships that could have appeared to influence the work reported in this paper.

Data availability

Data will be made available on request.

Acknowledgments

The authors would like to acknowledge the financial support from Interreg North-West Europe in the framework of the Cobracomp project (Nr. NWE885). The support from our project partners is gratefully acknowledged.

Appendix A. Computational algorithm of the single yarn-to-ring contact point model

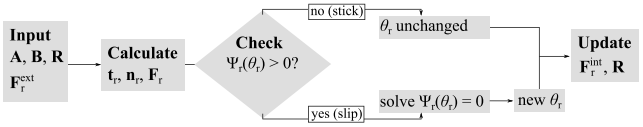

Fig. A.17. Flowchart of the predictor–corrector algorithm of the single yarn-to-ring contact point model.

Appendix B. Convergence study of the biaxial over-braiding simulation

See Fig. B.18.

Appendix C. Process parameters for the parametric studies

Table C.2
Process parameters for the parametric studies in Case A and Case B.

Case A	study 1	$\mu_{y(-)}$	0.0	0.1	0.2	0.3	0.4	0.5
		M_{int}(m)	0.4	0.4	0.4	0.4	0.4	0.4
	study 2	$\mu_{y(-)}$	0.3	0.3	0.3	0.3		
		M_{int}(m)	0.2	0.4	0.6	0.8		
Case B	study 1	$\mu_{y(-)}$	0.0	0.25	0.5			
		H_{int}(m)	0.2	0.2	0.2			

Appendix D. Sensitivity analysis of spool tension and yarn-to-ring coefficient of friction

Additional parametric studies were performed to study the effects of spool tension and yarn-to-ring coefficient of friction on the braid angle. The spool tension was varied using different values 2 N, 4 N, 6 N, 8 N while the other parameters were kept the same. Next, only the yarn-to-ring coefficient of friction was changed from 0.0, 0.2, 0.4 and 0.6. The parameters were shown in Table D.3. The average relative difference between the braid angles was calculated using the formula:

$$\mathrm{Diff} = \mathrm{average}\left(\frac{\alpha_{\mathrm{ref}} - \alpha}{\alpha_{\mathrm{ref}}}\right).100\% \tag{D.1}$$

where α_{ref} is the reference braid angles obtained from simulations using $f_{sup}^{ext} = 2\mathrm{N}$ and $\mu_r = 0.0$. The data indicated that changing the yarn-to-ring friction coefficient and spool tension had no effect on the braid angles with under 1% of relative difference.

Table D.3
Sensitivity analysis of spool tension and yarn-to-ring coefficient of friction.

f_{sup}^{ext}(N)	2_{ref}	4	6	8
Diff(%)	0.0	0.54	0.89	0.76
$\mu_{r(-)}$	0.0_{ref}	0.2	0.4	0.6
Diff(%)	0.0	0.81	1.01	0.95

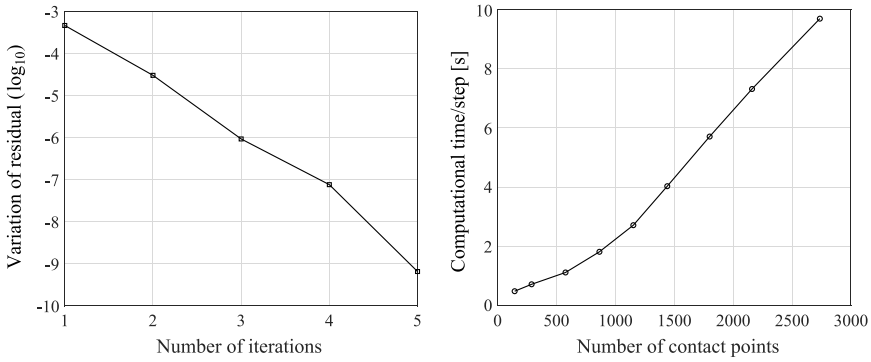

Fig. B.18. Convergence study of the biaxial over-braiding simulation: (left) relative change of the residual against number of iterations for each time step, (right) computational time with increasing number of contact points.

References

[1] Kyosev Y. Braiding Technology of Textiles. Woodhead Publishing; 2014.
[2] Kyosev Y. Advances in Braiding Technology. Woodhead Publishing; 2016.
[3] Branscomb D, Beale D, Broughton R. New directions in braiding. J Eng Fibers Fabrics 2013;11–24.
[4] Gries T, Veit D, Wulfhorst B. Textile Technology : An Introduction. Hanser; 2014.
[5] Kyosev Y. Recent Developments in Braiding and Narrow Weaving. Springer; 2016.
[6] Ayranci C, Carey J. 2D braided composites: A review for stiffness critical applications. Compos Struct 2008;85(1):43–58.
[7] Carey J. Handbook of Advances in Braided Composite Materials. Woodhead Publishing; 2017.
[8] Boisse P. Composite Reinforcements for Optimum Performance. Woodhead Publishing; 2011.
[9] Ko FK. Braiding. Engineered Materials Handbook, vol. 1. ASM International; 1987, p. 519.
[10] Kessels J, Akkerman R. Prediction of the yarn trajectories on complex braided preforms. Compos Part A: Appl Sci Manuf 2002;33(8):1073–81.
[11] Pickett AK, Sirtautas J, Erber A. Braiding simulation and prediction of mechanical properties. Appl Compos Mater 2009;16(6):345.
[12] Pickett A, Erber A, von Reden T, Drechsler K. Comparison of analytical and finite element simulation of 2D braiding. Plast Rubber Compos 2013;38:387–95.
[13] Hans T, Cichosz J, Brand M, Hinterhölzl R. Finite element simulation of the braiding process for arbitrary mandrel shapes. Compos Part A: Appl Sci Manuf 2015;77:124–32.
[14] Swery E, Hans T, Bultez M, Wijaya W, Kelly P, Hinterhölzl R, et al. Complete simulation process chain for the manufacturing of braided composite parts. Compos Part A: Appl Sci Manuf 2017;102:378–90.
[15] Sun X, Kawashita LF, Wollmann T, Spitzer S, Langkamp A, Gude M. Experimental and numerical studies on the braiding of carbon fibres over structured end-fittings for the design and manufacture of high performance hybrid shafts. Product Eng 2018;12(2):215–28.
[16] Wang X, Zhang G, Shi X, Zhang C. Study on the simulation of annular axis braiding process and braiding angles' prediction method. Compos Adv Mater 2021;30:26349833211010814.
[17] Del Rosso S, Iannucci L, Curtis PT. Finite element simulation of the braiding process. Mech Adv Mater Mod Process 2019;5(1):1.
[18] Monnot P, Lévesque J, Laberge Lebel L. Automated braiding of a complex aircraft fuselage frame using a non-circular braiding model. Compos Part A: Appl Sci Manuf 2017;102:48–63.
[19] van Ravenhorst J, Akkerman R. Circular braiding take-up speed generation using inverse kinematics. Compos Part A: Appl Sci Manuf 2014;64:147–58.
[20] Gondran M, Abdin Y, Gendreau Y, Khameneifar F, Laberge Lebel L. Automated braiding of non-axisymmetric structures using an iterative inverse solution with angle control. Compos Part A: Appl Sci Manuf 2021;143:106288.
[21] van Ravenhorst J, Akkerman R. A yarn interaction model for circular braiding. Compos Part A: Appl Sci Manuf 2016;81:254–63.
[22] Zhang Q, Beale D, Broughton RM. Analysis of circular braiding process, part 1: Theoretical investigation of kinematics of the circular braiding process. J Manuf Sci Eng 1999;121:345–50.
[23] Zhang Q, Beale D, Broughton RM, Adanur S. Analysis of circular braiding process, part 2: Mechanics analysis of the circular braiding process and experiment. J Manuf Sci Eng 1999;121:351–9.
[24] Cornelissen B, Rietman B, Akkerman R. Frictional behaviour of high performance fibrous tows: Friction experiments. Compos Part A: Appl Sci Manuf 2013;44:95–104.
[25] Tourlonias M, Bueno M-A, Poquillon D. Friction of carbon tows and fine single fibres. Compos Part A: Appl Sci Manuf 2017;98:116–23.
[26] Tourlonias M, Bueno M-A. Experimental simulation of friction and wear of carbon yarns during the weaving process. Compos Part A: Appl Sci Manuf 2016;80:228–36.
[27] Chakladar N, Mandal P, Potluri P. Effects of inter-tow angle and tow size on carbon fibre friction. Compos Part A: Appl Sci Manuf 2014;65:115–24.
[28] Cornelissen B, Sachs U, Rietman B, Akkerman R. Dry friction characterisation of carbon fibre tow and satin weave fabric for composite applications. Compos Part A: Appl Sci Manuf 2014;56:127–35.
[29] Mulvihill DM, Smerdova O, Sutcliffe MP. Friction of carbon fibre tows. Compos Part A: Appl Sci Manuf 2017;93:185–98.
[30] Tourlonias M, Bueno M-A, Fassi G, Aktas I, Wielhorski Y. Influence of friction angle between carbon single fibres and tows: Experimental analysis and analytical model. Compos Part A: Appl Sci Manuf 2019;124:105478.
[31] Du GW, Popper P. Analysis of a circular braiding process for complex shapes. J Text Inst 1994;85(3):316–37.
[32] Amontons G. De la résistance causée dans les machines. Mémoires de l'Académie Royale A; 1699, p. 257–82.